

CONTINUOUS DISTRIBUTION OF α t RELATIVE KINETIC ENERGIES IN ${}^7\text{Li}$ BREAKUP REACTIONS

H. UTSUNOMIYA, Y.-W. LUI, L. COOKE, H. DEJBAKSH, D.R. HAENNI,
P. HEIMBERG, A. RAY¹, B.K. SRIVASTAVA and R.P. SCHMITT

Cyclotron Institute, Texas A&M University, College Station, Texas 77843-3366, USA

T. UDAGAWA

Department of Physics, University of Texas, Austin, Texas 78712, USA

Received 21 August 1989

Abstract: A newly developed technique has been used to probe a previously inaccessible region of the continuum in the α t channels of ${}^7\text{Li}$ breakup reactions. This was used to investigate reactions of 63 MeV ${}^7\text{Li}$ with ${}^{58}\text{Ni}$, ${}^{120}\text{Sn}$, ${}^{144}\text{Sm}$, and ${}^{208}\text{Pb}$ targets. Breakup pairs of α -particles and tritons emitted within a finite opening angle were analyzed according to their magnetic rigidity using a $K=150$ Enge split-pole spectrograph. The α t coincidences were taken with two single-wire proportional counters mounted at different positions along the focal plane of the spectrograph. The large energy acceptance ($E_{\text{max}}/E_{\text{min}} \approx 8$) of the spectrograph is crucial to the present coincidence measurements involving two particles with different q/m values. Very small relative energy components were studied without any detection threshold. A pronounced bump was observed immediately above the α t particle threshold. No strong indication of the post Coulomb acceleration was observed. The excitation of the continuum states as well as the $\frac{7}{2}^-$ state in ${}^7\text{Li}$ is discussed in terms of the distorted-wave Born approximation. The astrophysical implications of the data are also discussed regarding the Coulomb excitation of the continuum. The present technique offers the promise of very high sensitivity at small relative energies if it were applied in conjunction with ray-tracing, a thin target, and a dispersion-matched beam.

E

NUCLEAR REACTIONS ${}^{208}\text{Pb}({}^7\text{Li}, {}^7\text{Li}), {}^{208}\text{Pb}({}^7\text{Li}, {}^7\text{Li}^*[\frac{1}{2}^-; 0.478 \text{ MeV}]), {}^{208}\text{Pb}({}^7\text{Li}, {}^7\text{Li}){}^{208}\text{Pb}[3^-; 2.61 \text{ MeV}], E=63 \text{ MeV}$; measured $\sigma(\theta)$. ${}^{208}\text{Pb}, {}^{144}\text{Sm}, {}^{120}\text{Sn}, {}^{58}\text{Ni}({}^7\text{Li}, \alpha t), E=63 \text{ MeV}$; measured $\sigma(E_\alpha, E_t, \theta)$. Enriched targets. Enge split-pole spectrograph. DWBA analysis. Nuclear astrophysics.

1. Introduction

Recently, there has been a growing interest in measuring two-particle correlations at very small relative energies, in conjunction with nuclear astrophysics^{1,2}). Experimentally, these small relative energies on the order of keV, have long been beyond the detection capability of conventional methods involving detector telescopes. The detection threshold, in large part, stems from the finite angle between detector telescopes and thus cannot be eliminated unless the telescopes are placed at the same angle³). This situation applies even to highly segmented detector systems such

¹ Present address: Oak Ridge National Laboratory, Oak Ridge, TN 37830, USA.

as the plastic ball⁴⁾). In addition to the detection threshold problem, a telescope is not generally suited to correlation measurements inside the grazing angle due to radiation damage arising from intense elastic scattering. This can be a serious disadvantage since correlation cross sections are often appreciable at forward angles.

A new technique which is well suited for probing the previously inaccessible regions of the relative energies has been developed recently^{5,6)}. It should be noted that the possibility of this technique was pointed out in the early 1960s during the pioneering days in the development of magnetic spectrographs⁷⁾. The technique, which utilizes a broad-range magnetic spectrograph, works best for pairs of particles with different charge-to-mass ratios. The principle behind the technique is simple. A pair of particles with zero relative velocity will be emitted at exactly the same angle in the laboratory frame. When they enter a magnetic field, the radii of the curvature depend only on their q/m values. Thus, a pair of particles with different q/m values will be focused at different positions along the focal plane. If the momentum acceptance of the magnetic spectrograph is sufficiently large, a coincidence measurement is feasible using two focal plane detectors mounted in the appropriate positions along the focal plane. Obviously, this method also avoids the interference from the elastic scattering. If the two particles have identical q/m value, the threshold cannot be completely eliminated. In this case, extra effort is required to minimize the dead space between two focal plane detectors in order to observe small relative energies. In the event that one of the particles is a neutron, a detection threshold free measurement is still feasible in combination with time-of-flight measurements of the neutrons using the 0° port of the spectrograph.

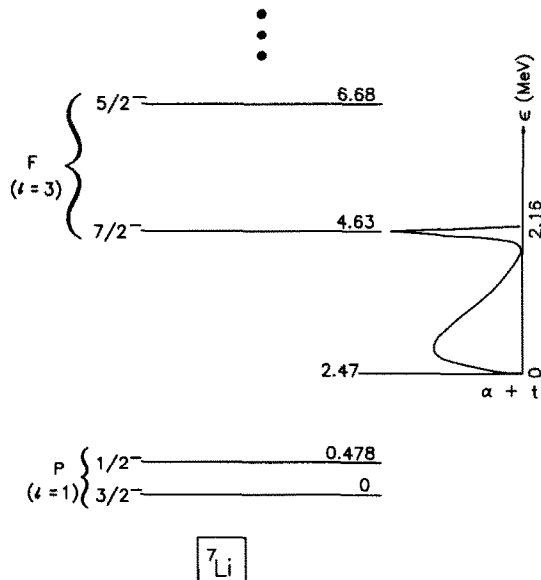


Fig. 1. Low-lying nuclear levels of ${}^7\text{Li}$. The region of interest in the present study is indicated.

This paper details an application of the spectrograph technique to ${}^7\text{Li}$ breakup reactions at 63 MeV. The present α t coincidence measurements covered the excitation energy of ${}^7\text{Li}$ from the α t separation energy at 2.47 MeV to the $\frac{7}{2}^-$ state at 4.63 MeV (see fig. 1). In the next section, the experimental method is discussed. The results are presented in sect. 3. We note that there are some differences between these results and those presented previously⁶⁾. Discussions of DWBA analyses and nuclear astrophysical applications are given in sect. 4. Sect. 5 summarizes the conclusions of this work.

2. Experimental procedure

2.1. BEAM AND TARGET

A beam of 63 MeV ${}^7\text{Li}$ was produced by the 88" cyclotron at Texas A&M University. Self-supporting metallic foils of ${}^{208}\text{Pb}$ (10.6 mg/cm²), ${}^{144}\text{Sm}$ (4.63 mg/cm²), ${}^{120}\text{Sn}$ (7.88 mg/cm²), and ${}^{58}\text{Ni}$ (11.4 mg/cm²) were irradiated. The beam spot on target was less than 2×2 mm². The beam current was integrated using a Faraday cup mounted inside a scattering chamber. The beam intensity on target ranged from 50 to 200 enA.

2.2. MAGNETIC SPECTROGRAPH

The experimental setup is schematically shown in fig. 2. The α -particles and tritons emitted at essentially the same laboratory angle entered an Enge split-pole

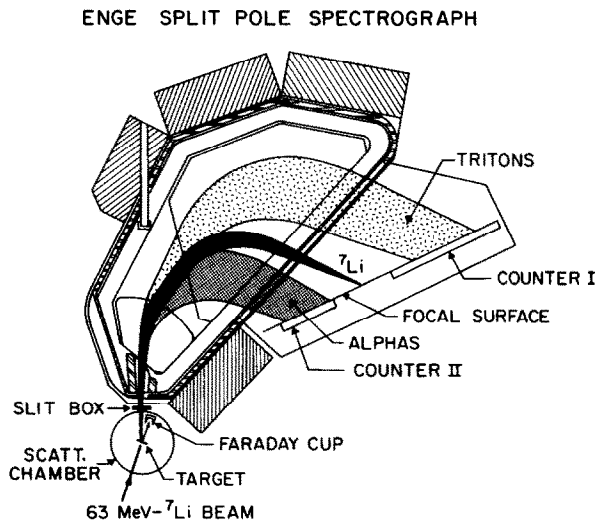


Fig. 2. Layout of the experimental setup.

spectrograph⁸⁾ and were analyzed according to their magnetic rigidity. Because of their different q/m ratios the particles were focused at different positions along the focal plane. The energy-mass product (K -value) of the spectrograph was 150. The nominal range of the radius of the curvature (ρ) was 400–1100 mm. During the runs the magnetic field was set at 14.91 kG. Two kinds of spectrograph apertures were used, 3.0 and 5.3 msr. The latter setting was used most of the time. Single-wire proportional counters of 86 cm and 40 cm in length were mounted in the ρ -ranges 440–600 mm and 775–1090 mm, respectively. Both detectors were backed by NE102A plastic scintillators. This set-up favored the detection of coincident forward-going tritons and backward-going α -particles in the projectile frame (see the velocity diagram shown in fig. 3). The α -particles and tritons were cleanly separated from other particles in a 2-dimensional plots of the energy loss (ΔE) in the proportional counter versus the position. Elastically scattered ^7Li impinged on a gap between the two counters and thus caused no interference in the coincidence measurements.

2.3. HORIZONTAL AND VERTICAL MAPPING

Since the focal plane of the split-pole spectrograph is slightly curved⁸⁾, it is not possible to achieve the best position resolution for both individual focal plane detectors, which were mounted in the high $B\rho$ and low $B\rho$ sides, respectively. We arrived at the best compromise in resolution by means of horizontal mapping of the focal surface. This procedure automatically corrected for the higher order aberration, which is important for the present measurements with the large solid angles of the spectrograph. The split-pole spectrograph is not a perfect stigmatic-focusing instrument despite the good performance of the vertical-focusing over the whole range⁸⁾. The maximum collecting power was achieved by adjusting the vertical position of the focal plane.

2.4. ENERGY AND EFFICIENCY CALIBRATIONS OF THE FOCAL PLANE DETECTOR

Since the goal of this study was the measurement of continuum α t pairs at very low relative kinetic energies, the energy calibration of the two focal plane detectors was critical to the experiment. The energy calibration involved a two-fold procedure. First, the energy of an α -beam (nominal energy 35 MeV) was accurately determined

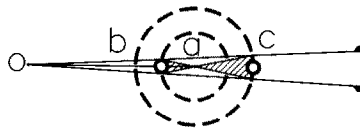


Fig. 3. Schematic velocity diagram for the spectrograph method of measuring two particle correlations. In the present experiment, $a = ^7\text{Li}$, $b = \alpha$ and $c = \text{triton}$.

using the crossover method for $^{12}\text{C}(\alpha, t)^{13}\text{N}$ and $^{12}\text{C}(\alpha, d)^{14}\text{N}$ reactions. The crossover of the triton and deuteron peaks was observed at 57.2° , yielding an absolute energy of $35.5 \text{ MeV} \pm 50 \text{ keV}$. Second, the α -beam was used to calibrate the 86 cm triton counter with $^{27}\text{Al}(\alpha, t)^{28}\text{Si}(0^+, 2^+, 4^+)$ reactions and the 40 cm α -counter with $^{12}\text{C}(\alpha, \alpha')^{12}\text{C}(0_1^+, 2^+, 0_2^+, 3^-)$ reactions. The absolute energies of α -particles and tritons were thus obtained to an accuracy of 1%.

The efficiency calibration was studied for both the alpha and triton detectors. Since the alpha detector covers the low $B\rho$ region of the spectrograph which was seldom used, an independent measurement of $^{208}\text{Pb}(\alpha, \alpha')^{208}\text{Pb}$ reactions were made with both the spectrograph and a silicon detector telescope. Comparing these two results, the detection efficiency was found to be 100% within an accuracy of 10% over the entire p -range covered. Similar efficiency was obtained for the triton counter on the high $B\rho$ side of the spectrograph. Thus, the systematic error in the coincidence efficiency is about 10%. The overall uncertainties in the absolute cross sections are estimated to be less than 20%.

2.5. TAC SPECTRA

Time spectra were generated from the signals from the two plastic scintillators in the back of the α and triton detectors. Fig. 4 shows a typical TAC spectrum gated on both α -particles and tritons. There are two points to note regarding this spectrum. First, the true-to-random ratio is relatively small. However, it is drastically improved by gating on a special kinematical solution called elastic breakup (see next section). This is illustrated in fig. 3. The coincidence phase space selected by the present

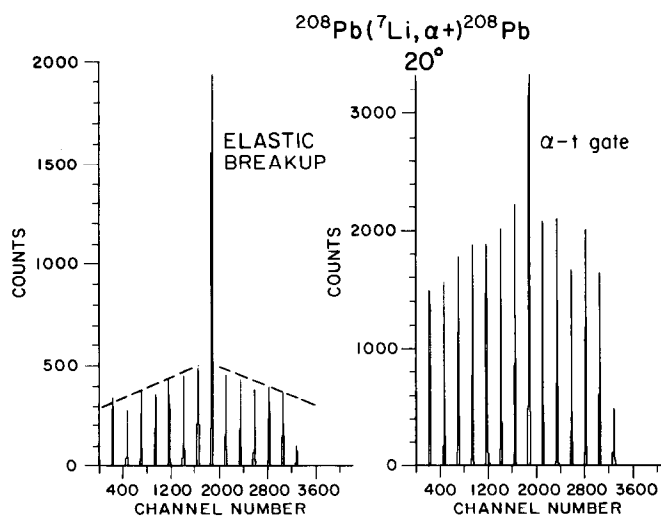


Fig. 4. TAC spectra gated on elastic breakup and on all αt coincidences. The dashed line is to guide the eye.

technique is a fairly small fraction of the total events (generally smaller than would be observed with the telescope method). Uncorrelated (singles) breakup events producing beam-velocity α -particles and tritons provide an intense background of the random events. These are largely eliminated by gating the elastic breakup pairs. A second noteworthy feature of the time spectrum is the approximately linear decrease in random events with increasing time between the two beam pulses. This linear trend, which was observed for a time period of $\pm 1 \mu\text{s}$ around the true peak, is known to be associated with the poor duty cycle of the accelerator ^{9,10}). As pointed out in ref. ⁹), a small fluctuation in the D -voltage can produce a poor duty cycle if the beam energy is tightly regulated by a magnetic analyzing system. Assuming that the beam had a periodic time structure ¹⁰) and that each pulse contained the same number of beam particles, we estimate that there were typically 25–30 beam pulses per macrocycle. The number of missing beam pulses could not be accurately determined because the time range of the TAC module ($2 \mu\text{s}$) was not sufficiently long to determine it. The linear trend in randoms was taken into account in the subtraction of the random coincidences.

2.6. ELASTIC AND INELASTIC SCATTERING

In addition to the coincidence runs, elastic scattering and inelastic scattering of 63 MeV ^7Li on a ^{208}Pb target were also studied. In the inelastic scattering data, the excitation of ^7Li to its $\frac{1}{2}^-$ state at 0.48 MeV and the excitation of ^{208}Pb to the 3 state at 2.6 MeV were observed with the spectrograph. The measurements were made with a $300 \mu\text{g}/\text{cm}^2$ thick ^{208}Pb foil and a 0.33 msr solid angle of the spectrograph.

3. Results

3.1. ELASTIC AND INELASTIC SCATTERING

Fig. 5 shows the angular distribution of ^7Li elastically scattered from ^{208}Pb at 63 MeV. The angular distributions for inelastic scattering leading to the $\frac{1}{2}^-$ state in ^7Li and the 3^- state in ^{208}Pb are shown in fig. 6. Starting with the parameters of ref. ¹¹), an optical potential was determined by χ^2 -fitting of the elastic scattering data. The best-fit parameters are summarized in table 1. The quantities underlined in the table were fixed in the χ^2 -fitting procedure.

3.2. 2-DIMENSIONAL PLOTS OF αt COINCIDENCE EVENTS

Fig. 7 shows a 2-dimensional plot of αt coincidence events measured at 15° with a ^{208}Pb target. This figure was generated by gating on the “true” peak (see fig. 4) in the TAC spectrum, which also contains random coincidences from the same beam pulse. One can see that nuclear events exhibit a strong concentration along

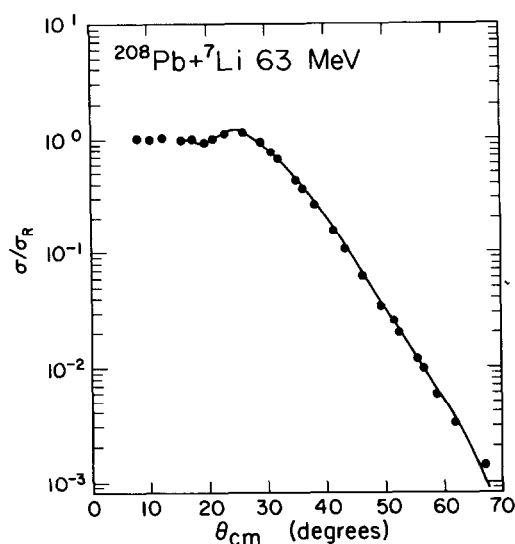


Fig. 5. Rutherford ratios for the elastic scattering angular distributions. The solid line represents the χ^2 fit (see text).

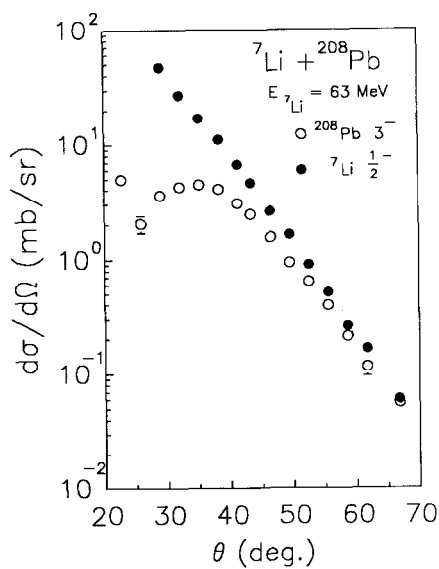


Fig. 6. Inelastic scattering angular distributions in the $^{208}\text{Pb} + ^7\text{Li}$ reactions at 63 MeV, leading to the $\frac{1}{2}^-$ state of ^7Li at 0.478 MeV (filled circles) and the 3^- state of ^{208}Pb at 2.61 MeV (open circles).

TABLE 1
Optical potential parameters for the ${}^7\text{Li} + {}^{208}\text{Pb}$ system at $E_{\text{lab}}({}^7\text{Li}) = 63$ MeV deduced from the χ^2 fit to the elastic scattering data

V (MeV)	a_R (fm)	r_R (fm)	W (MeV)	a_I (fm)	r_I (fm)	r_c (fm)
244	<u>0.65</u>	1.45	12.0	<u>0.90</u>	1.68	<u>1.40</u>

a kinematical locus corresponding to a constant value of the sum of α and triton energies. The energy sum can be written as $E_\alpha + E_t = E_0 + Q - E_3$. Here, E_0 is the bombarding energy, Q is the reaction Q -value, and E_3 is the recoil kinetic energy of the target nucleus. The observed kinematical locus corresponds to elastic breakup in which the target nucleus stays in the ground state, namely, $Q = -S$, where S is the separation energy of ${}^7\text{Li}$ into an α and a triton. The energy sum is constant nearly independent of the detection angle because the recoil energy is fairly small. The majority of the random coincidence events are seen near α and triton energies corresponding to the beam velocity. This indicates that the randoms stem from uncorrelated singles breakup events as noted above.

Fig. 8 shows 3-dimensional plots for all the targets taken at 12° . Elastic breakup events are clearly seen in the plots for the ${}^{144}\text{Sm}$ and the ${}^{120}\text{Sn}$ targets as well. The elastic breakup was *exclusively* observed for ${}^{208}\text{Pb}$ and ${}^{120}\text{Sn}$ targets in the entire

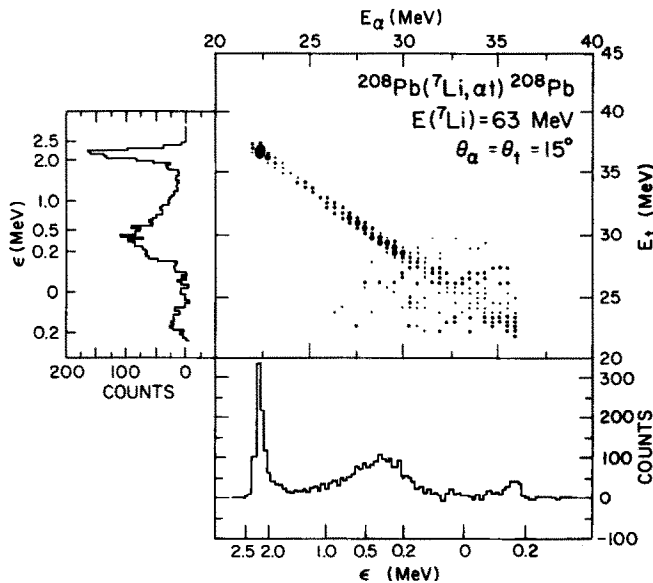


Fig. 7. Two-dimensional plots of αt correlations observed at 15° in ${}^{208}\text{Pb} + {}^7\text{Li}$ reactions at 63 MeV. The projected spectra on the α and triton energy axes are also given.

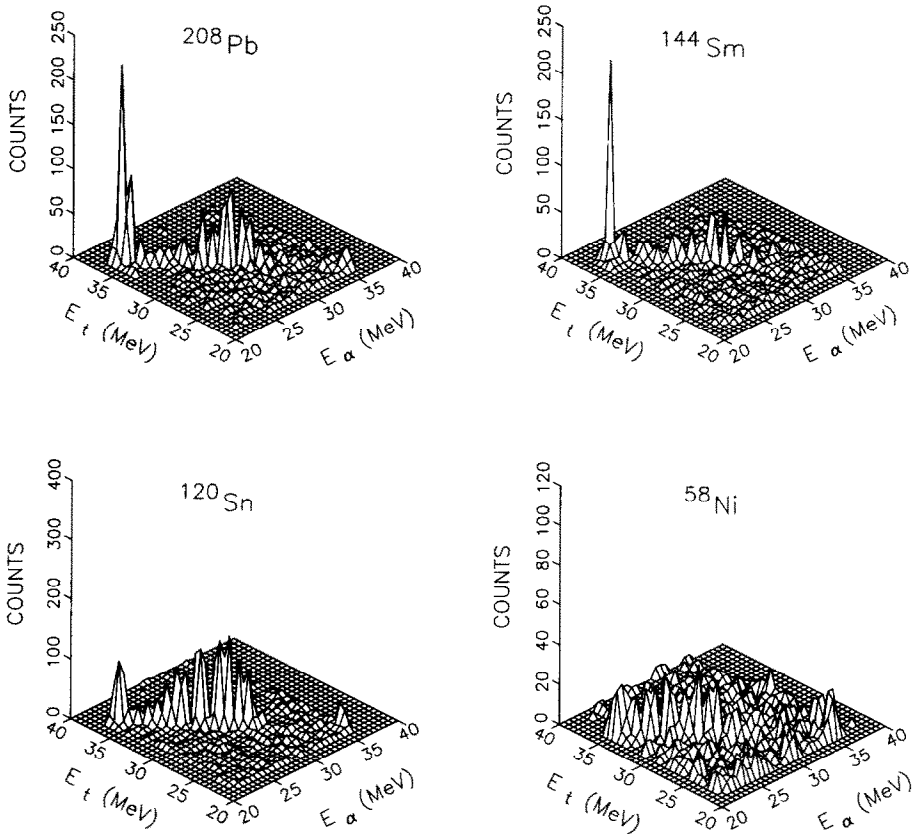


Fig. 8. Three-dimensional plots of αt correlations observed at 12° in the ^7Li -induced reactions with ^{208}Pb , ^{144}Sm , ^{120}Sn , and ^{58}Ni targets.

angular range, namely, $9\text{--}50^\circ$, and for ^{144}Sm at 15° , the only angle at which the measurement was made for this target. The ^{58}Ni target was only studied at 12° . In contrast to the other targets, inelastic breakup was found to dominate at this particular angle for ^{58}Ni . In this case, the target nucleus is excited to the 2^+ state at 1.45 MeV.

3.3. CONTINUUM αt SPECTRA AND THE $\frac{7}{2}^-$ STATE AT 4.63 MeV

Nuclear events corresponding to elastic and inelastic breakup were corrected for randoms and projected to form 1-dimensional α - and t -spectra (see fig. 7). Sharp peaks are observed in the projected spectra. In the ^{208}Pb measurement the peaks at $E_\alpha = 22$ MeV and $E_t = 36$ MeV arise from the decay of the $\frac{7}{2}^-$ state of ^7Li at 4.63 MeV. The relative kinetic energy between an α and a triton was calculated assuming that the ^7Li is inelastically excited in the field of the target and subsequently decays into an α and a triton. The αt relative energy scale is shown in fig. 7. The locations of

the sharp peaks coincide well with the value of the relative kinetic energy corresponding to the $\frac{7}{2}^-$ state (2.16 MeV). This component has been previously observed¹²⁾ in the breakup of 70 MeV ^7Li .

Besides the decay of the $\frac{7}{2}^-$ state, a continuous distribution of the α t relative energies (ε), is observed (see fig. 7). Continuum structures have also been seen in telescope measurements¹²⁾. However, the experimental setup resulted in a detection threshold at $\varepsilon = 290$ keV. The present method covered the entire range of the relative kinetic energies from zero to 2 MeV, avoiding the effect of detection thresholds. The entire continuum bump was observed for all targets in the elastic breakup on ^{208}Pb , ^{144}Sm , and ^{120}Sn as well as in the inelastic breakup on ^{58}Ni .

3.4. LOCATION OF THE SPECTRAL MINIMA

Although the present experimental setup favored the detection of the forward-going tritons and backward-going α particles in the projectile frame, the forward-going α 's and backward-going tritons were also observed over a limited range of ε , about 200 keV. Thus, the actual minima of the alpha and triton energy distributions were observed. The minima should correspond to the exotic situation in which the breakup takes place with zero relative energy. The Coulomb field of the target can shift the location of this minima according to its strength at the breakup point^{13,14)}. It is thus important to examine the data to look for possible post breakup acceleration effects which could provide insight into the reaction mechanism.

Parameterizing the Coulomb field of the target at the ^7Li breakup in terms of the potential energy per unit charge, V_c , the α and triton energies at $\varepsilon = 0$ in the laboratory frame can be expressed as $E_\alpha = \frac{4}{7}W + \frac{2}{7}V_c$ and $E_t = \frac{3}{7}W - \frac{2}{7}V_c$, respectively. Here, W is the sum of the α and triton energies, which is a constant for elastic and inelastic breakup, as mentioned above. The α particles are accelerated to an energy, $\frac{2}{7}V_c$, above that obtained in the absence of a Coulomb field. In contrast, the tritons are decelerated by the same amount. This arises because the charge-to-mass ratio of an α particle (a triton) is larger (smaller) than that of ^7Li .

The nuclear events around the spectral minima are shown in figs. 9 and 10. Using the most probable value of W obtained from the event by event analysis, the values of E_α ($\frac{4}{7}W$) and E_t ($\frac{3}{7}W$) assuming no Coulomb acceleration ($V_c = 0$) were obtained. These are indicated by the arrows labeled A. One immediate observation can be made from the location of the minima. If the breakup took place at the nuclear surface of the target, V_c should be about 10 MeV for ^{208}Pb , 8.3 MeV for ^{144}Sm , 7.0 MeV for ^{120}Sn , and 4.6 MeV for ^{58}Ni . The corresponding shifts, $\frac{2}{7}V_c$, in the zero relative energy are clearly inconsistent (too large) with the location of the minima in all cases. This seems to exclude the prompt breakup of ^7Li at the instant the projectile and the target overlap.

It is difficult to precisely pinpoint breakup acceleration effects for two reasons.

(1) The present data do not fully cover the region of forward-going alphas and

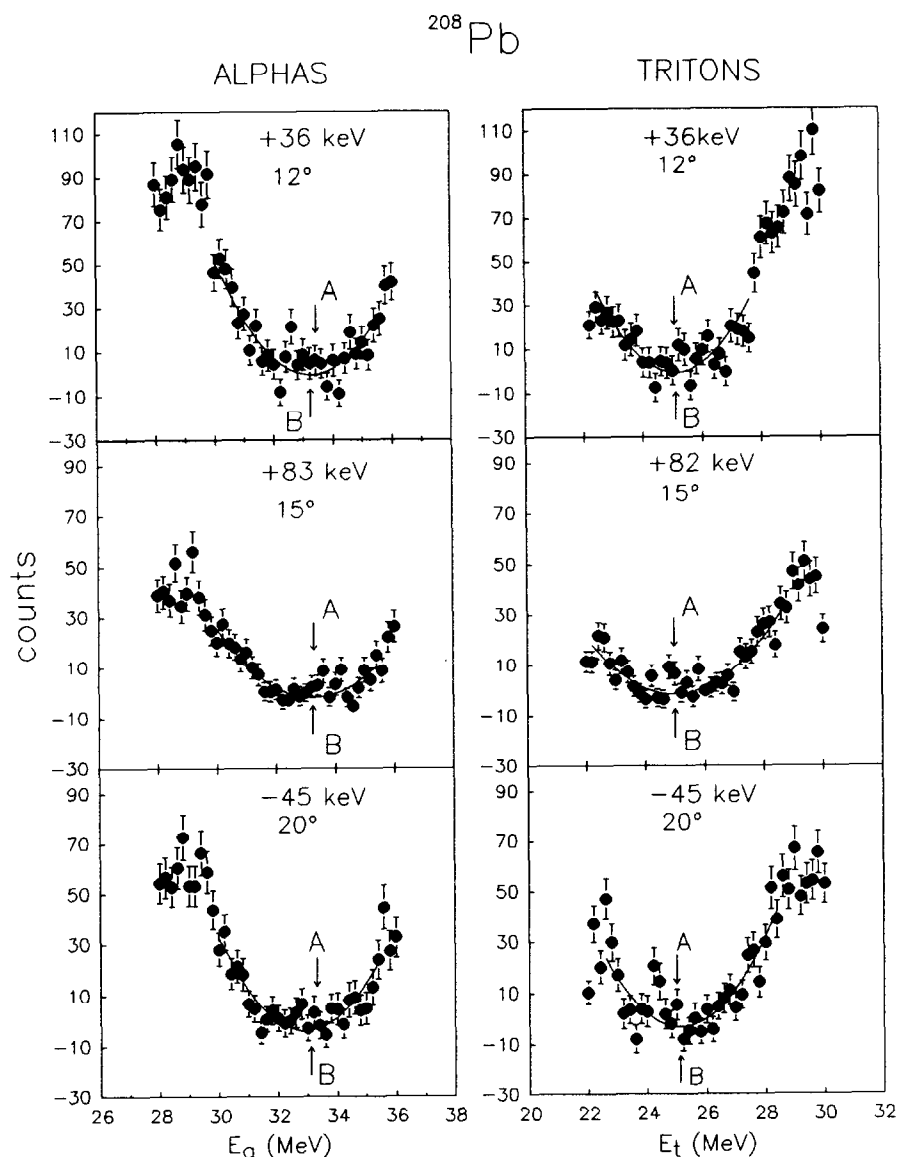


Fig. 9. Coincidence spectra of α -particles and tritons around $\varepsilon = 0$ taken with a ^{208}Pb target. The solid lines represent the χ^2 fitting with a quadratic power curve. The energy shifts obtained in the present analyses are also given. See text for significance of arrows labeled A and B and additional details.

backward-going tritons, so it is not possible to see possible distortion effects in the spectrum. (2) The cross sections around $\varepsilon = 0$ are close to zero due to the Coulomb barrier between the α and the triton, making it difficult to obtain adequate statistics for precise determinations of the minimum. Nevertheless, an attempt was made to locate the spectral minima by a χ^2 -fitting of the α and the triton spectra. A quadratic

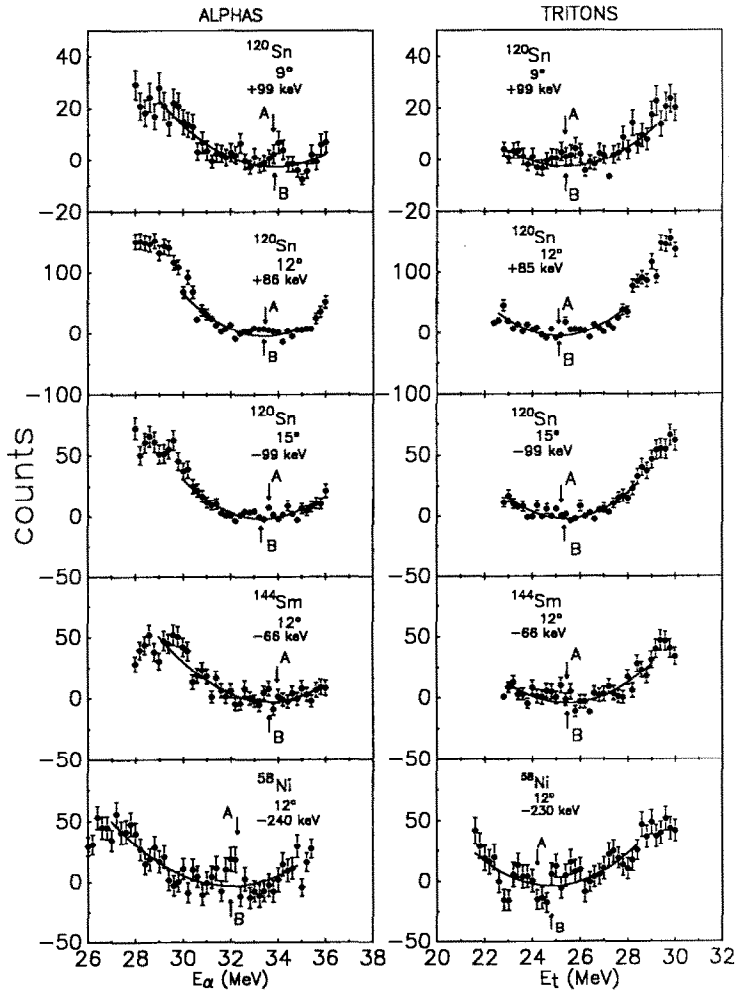


Fig. 10. Similar to fig. 9 for the ^{120}Sn , ^{144}Sm , and ^{58}Ni targets.

power law was used to locate the minima in restricted regions of the spectra. The best fit values of the spectral minima, E_0 , are indicated by the arrows labeled B in figs. 9 and 10. Note that the location of the spectral minima thus obtained is very close to that corresponding to $V_c=0$ (the arrow labeled A), but unrealistically indicating negative values for V_c . Facing this puzzling result, we carefully examined the effects of the energy losses of the alpha and the triton in the target. We obtained the value of W in the middle of the target material by correcting for the energy losses. Letting the α and the triton share W in proportion to their masses, we obtained the corrected α - and t-energies after passing through the target foil. The resulting energy shifts corresponding to $\frac{2}{7}V_c$ are also given in figs. 9 and 10. A positive

value is consistent with a repulsive potential. With the exception of the ^{58}Ni data for inelastic breakup, positive and negative shifts in the range of ± 100 keV are obtained with about equal frequency. Within an accuracy on the order of 100 keV, which may represent the limitation of the present analyses, the results strongly suggest that the pair of an α -particle and a triton do not suffer any significant Coulomb distortion effect, i.e., $V_c \leq 350$ keV. This removes some of the complications in obtaining the relative energy distributions. It is interesting to note that the present results on the post Coulomb acceleration are inconsistent with breakup at the distance of closest approach for a classical Coulomb trajectory. For instance, the distance of closest approach at 12° for ^{208}Pb is about 30 fm, giving $V_c = 3.9$ MeV. The resulting energy shift of 1 MeV is one order of magnitude larger than observed. The present observation seems to indicate a finite lifetime of the continuum states comparable to that of the resonant $\frac{7}{2}^-$ state. Thus, although the excitation of the continuum may take place in the vicinity of the target via the nuclear and/or Coulomb interactions, the decay seems to occur quite far away from the target, possibly indicating the importance of the final-state interaction between α and t.

3.5. α t RELATIVE-ENERGY DISTRIBUTIONS

The relative energy was determined, event by event, according to the relationship

$$\varepsilon = p_{\text{rel}}^2 / 2\mu, \quad (1)$$

where the relative momentum is

$$p_{\text{rel}} = \mu(p_\alpha / m_\alpha - p_t / m_t). \quad (2)$$

Here μ is the reduced mass of the α t system, m_α and m_t are the masses of an α and a triton, and, finally, p_α and p_t are the α - and the t-momentum, respectively. The kinematical transformation of the cross section, $d\sigma/dE_\alpha dE_t d\Omega_\alpha d\Omega_t$ (laboratory frame), to the cross section, $d\sigma/d\varepsilon d\Omega_{\alpha t} d\Omega_{Li}$ (projectile frame), followed the prescription given in ref. ¹⁵). Appendix A summarizes the kinematical details. The α t relative-energy distribution at 12° for ^{208}Pb is shown in fig. 11. In the transformation the emission angles of α -particles and tritons, θ_α and θ_t , were assumed to be 12° , and the post Coulomb acceleration was assumed to be zero.

The effects of the finite opening angle of the magnetic spectrograph were examined experimentally at 12° for ^{208}Pb using 5.3 msr and 3.0 msr solid angles. Fig. 12 shows the α t spectra taken with these two different solid angles, again using θ_α and θ_t equal to 12° . Some noticeable difference occurs around $\varepsilon = 500$ keV, but it is within the statistical errors. The finite-angle effect on the kinematical transformation was examined using different angles for the breakup partners (as determined by the aperture of the spectrograph). Four combinations of $\theta_\alpha = \theta_0 \pm \Delta\theta$ and $\theta_t = \theta_0 \pm \Delta\theta$

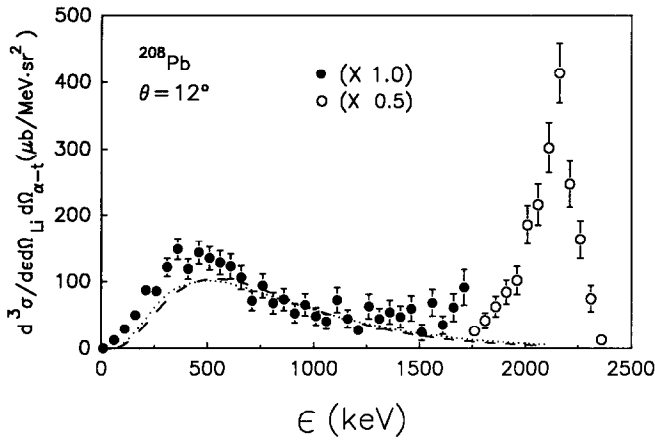


Fig. 11. αt relative energy distribution for ^{208}Pb at 12° taken with a 3.0 msr collimator. The dashed and dotted curves represent the Coulomb excitation calculations with astrophysical S -factors given by ref. ²⁶⁾ and ref. ²⁷⁾, respectively (see text). Normalization factors of 0.75 and 0.85 are introduced to the dashed and dotted curves, respectively.

were examined, where θ_0 is the central angle of the spectrograph collimator and $\Delta\theta$ is half-angle opening. The results for the $\Omega = 5.3$ msr aperture ($\Delta\theta = 2.1^\circ$) at $\theta_0 = 12^\circ$, are shown in fig. 13. All four cases give essentially identical results, i.e., a small enhancement below 500 keV compared to the results obtained with $\theta_\alpha = \theta_t = 12^\circ$ and $\Delta\theta = 0^\circ$.

The effect of the finite target thickness on the relative energy distribution was also examined assuming that the breakup occurred in the middle of the target. By

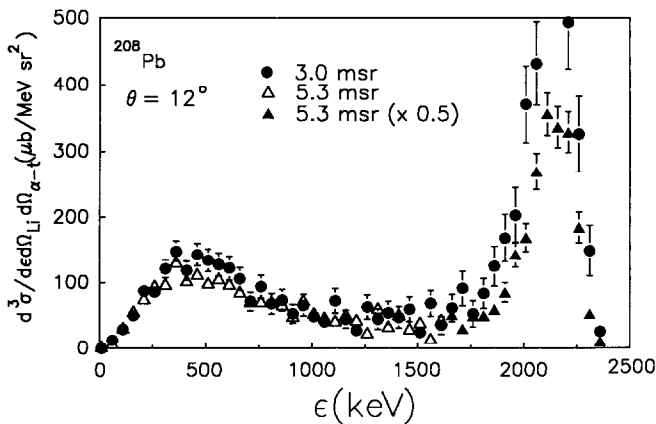


Fig. 12. Comparison of αt relative energy distributions for ^{208}Pb at 12° taken with a 3.0 msr collimator (filled circles) and a 5.3 msr collimator (open and filled triangles).

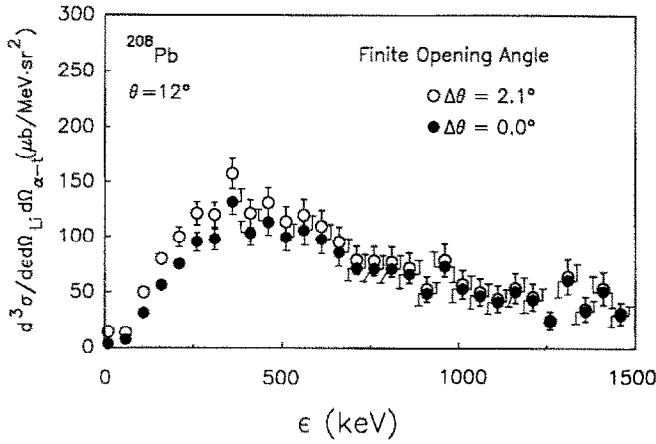


Fig. 13. Illustration of the effects of the finite opening angle on the kinematical transformation into the projectile frame. Using the data taken at 12° with a 5.3 msr collimator for ^{208}Pb , the relative energy distributions were obtained by setting $\theta_\alpha = \theta_t = 12^\circ$ (filled circles) and by setting $\theta_\alpha = 12^\circ \pm \Delta\theta$ and $\theta_t = 12^\circ \pm \Delta\theta$, where $\Delta\theta = 2.1^\circ$ (open circles).

correcting for the energy losses for every αt pair passing through the target, the relative energy distribution was reconstructed event by event. The result is shown in fig. 14 for the ^{208}Pb data obtained at 12° . One can see that this effect is negligible under the present experimental conditions.

Figs. 15–17 show the relative energy spectra at different angles and for various targets. Note that the spectrum for ^{58}Ni (the inelastic breakup) lacks the $\frac{7}{2}^-$ peak

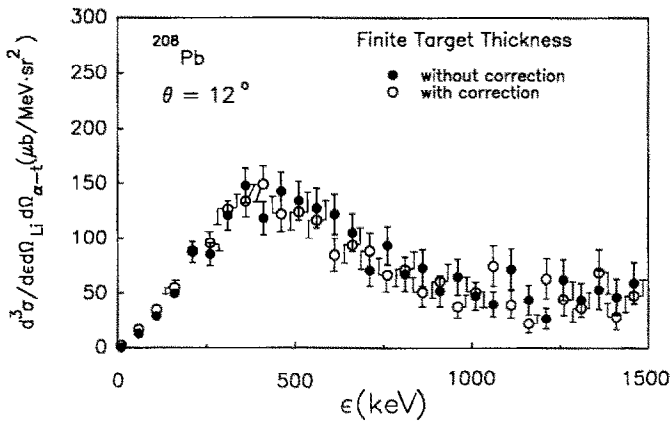


Fig. 14. Open circles give the αt relative energy distribution for ^{208}Pb at 12° corrected for the finite target thickness (11.6 mg/cm^2). The uncorrected spectrum is shown by the filled circles. See text for details.

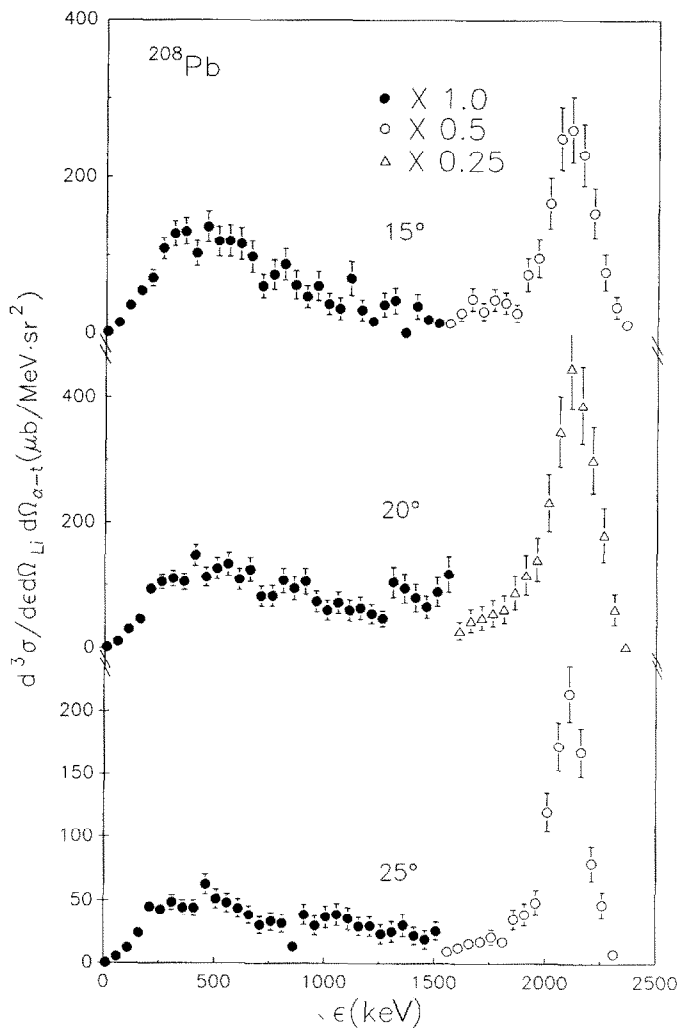


Fig. 15. Relative energy distributions for elastic breakup at 15°, 20°, and 25° taken with ^{208}Pb .

because it was outside the dynamic range spanned by the two focal plane detectors. It seems that the shape of the continuum observed for the inelastic breakup channel is quite different from that seen in the elastic breakup.

3.6. RELATIVE-ENERGY RESOLUTION

The resolution of the relative energy is determined mainly by two factors: (1) the finite opening angle, and (2) the finite target thickness. The effect of the spread in

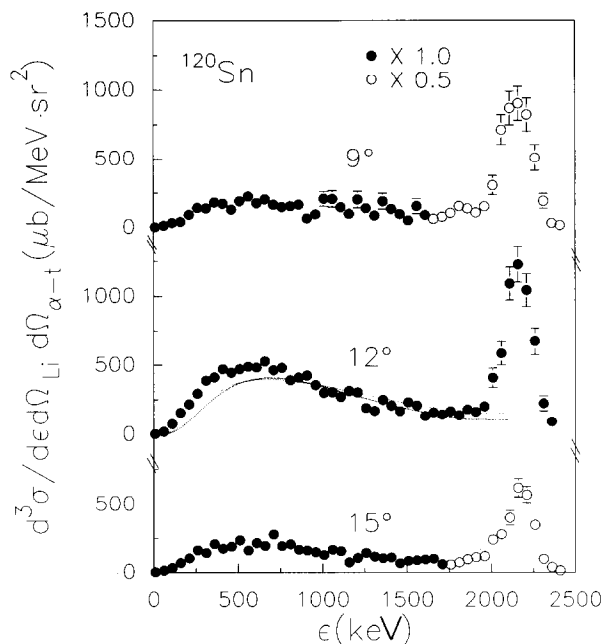


Fig. 16. Relative energy distributions for elastic breakup at 9°, 12°, and 15° taken with ^{120}Sn .

the beam energy is negligible because the ^7Li beam energy was tightly selected by an analyzing magnet. The effect of the beam width ($<2\text{ mm}$) on target can also be ignored because the horizontal magnification of the split pole spectrograph is about $\frac{1}{3}$.

The finite opening angle effect can be evaluated as follows⁵⁾. As seen in fig. 3, the α and triton are emitted over a range of angles in the projectile frame, determined by the solid angle of the spectrograph. For a fixed value of ϵ , this produces a finite spread in position along the focal plane. The energy resolution can be represented by $\Delta\epsilon/\epsilon$, where $\Delta\epsilon$ is the change in ϵ required to produce an observable change in the position along the focal plane. Fig. 18 shows the energy resolution expected for the 5.3 msr and 3.0 msr solid angles. The intrinsic resolution for zero solid angle was also calculated assuming 1 mm position resolution of the focal plane detectors. As the relative energy decreases, the resolution degrades since the maximum emission angle in the projectile frame becomes large. A critical energy can be defined below which α particles and tritons emitted at all angles in the projectile frame enter the spectrograph. Obviously, the resolution becomes very poor around this critical value. The critical energy is 60 keV for the 5.3 msr collimator and 34 keV for the 3.0 msr collimator.

The finite target thickness effect was evaluated by comparing the following cases in which the breakup takes place (1) at the front, (2) in the middle, and (3) at the back of the target foil. The energy spread in ϵ was calculated in cases (1) and (3)

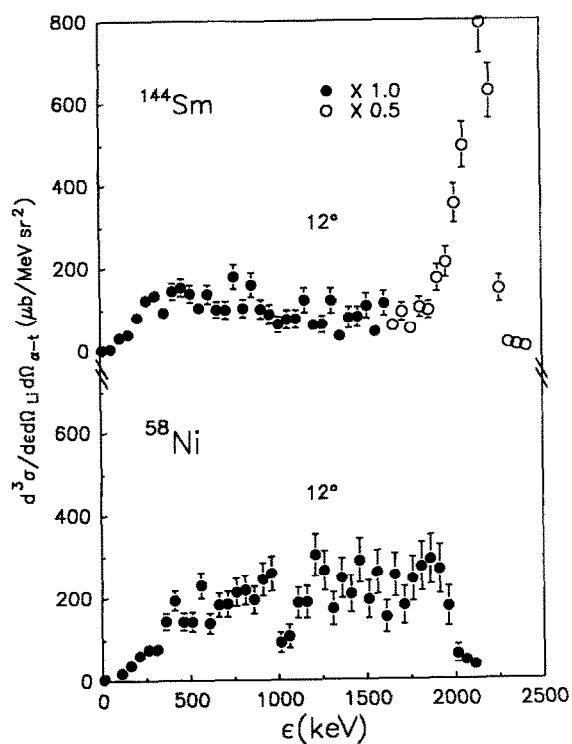


Fig. 17. Relative energy distributions for elastic breakup at 12° taken with ^{144}Sm (top) and for inelastic breakup at 12° taken with ^{58}Ni (bottom).

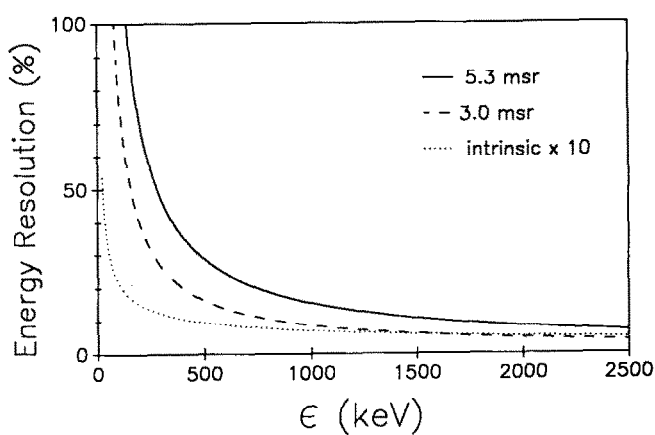


Fig. 18. Relative energy resolution as a function of relative energy for different opening angles of the spectrograph. For details, see text.

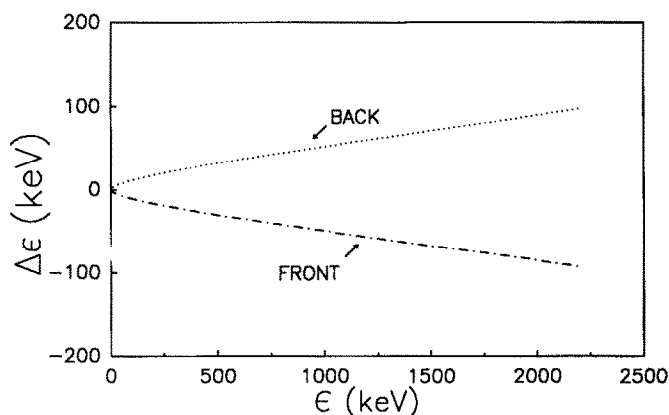


Fig. 19. Energy spread in relative energy due to the finite target thickness (10.6 mg/cm^2) of a ^{208}Pb target (see text).

relative to case (2). Fig. 19 shows the results for a 10.6 mg/cm^2 ^{208}Pb target and $\theta = 12^\circ$.

Table 2 compares the calculations with the observed widths of the $\frac{7}{2}^-$ peak. The experimental widths were obtained by fitting the $\frac{7}{2}^-$ peak with a gaussian function. The measured full widths at half maximum are roughly twice as broad as that observed in the $^6\text{Li}(\text{d}, \text{p})^7\text{Li}$ reaction ($93 \pm 8 \text{ keV}$)¹⁶). It seems that the full width at a tenth maximum is comparable to a coherent sum of these two leading factors.

3.7. ANGULAR DISTRIBUTION

Figs. 20 and 21 show angular distributions, $\text{d}\sigma/\text{d}\Omega_{\text{Li}}$, for the $\frac{7}{2}^-$ state and the continuum states. It was assumed that the α and the triton were emitted isotropically

TABLE 2
Widths of the resonant $\frac{7}{2}^-$ state in ^7Li for ^{208}Pb at 12°

Ω (msr)	FWHM (keV)	FWTM ^{a)} (keV)	$\Delta\epsilon_1$ ^{b)} (keV)	$\Delta\epsilon_2$ ^{c)} (keV)	$\Delta\epsilon_3$ ^{d)} (keV)	$\Delta\epsilon_{\text{all}}$ ^{e)} (keV)
5.3	213	389	177	186	11	374
3.0	192	350	98	186	11	295

^{a)} Full width at a tenth of the maximum.

^{b)} The contribution from the finite opening angle of the magnetic spectrograph.

^{c)} The contribution from the finite thickness (10.6 mg/cm^2) of the ^{208}Pb target.

^{d)} The contribution from the intrinsic position resolution (1 mm) of the focal plane detector.

^{e)} A coherent sum, i.e., $\Delta\epsilon_{\text{all}} = \Delta\epsilon_1 + \Delta\epsilon_2 + \Delta\epsilon_3$.

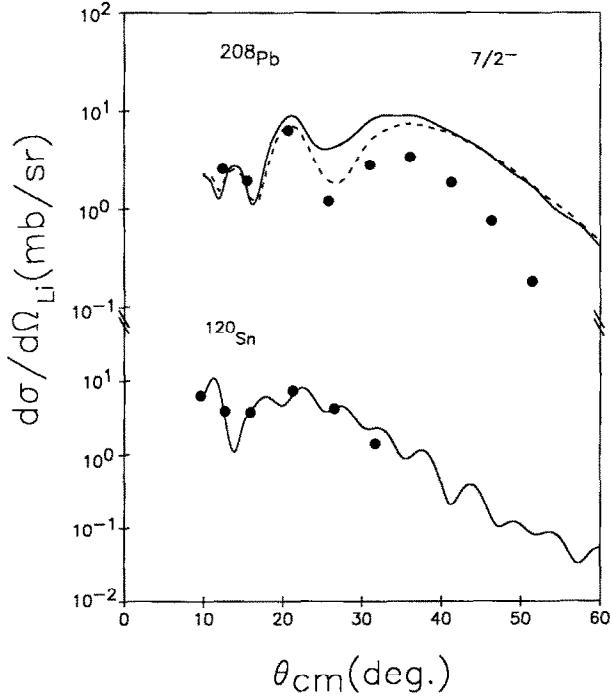


Fig. 20. Angular distributions of the resonant $\frac{7}{2}^-$ state of ${}^7\text{Li}$ taken with ${}^{208}\text{Pb}$ and ${}^{120}\text{Sn}$ targets. The solid curves represent the DWBA calculations with the collective E2 form factors $\beta_n = \beta_c = 0.098$. The dashed curve was obtained with $\beta_n/\beta_c = 1.5$ and $\beta_c = 0.098$. The normalization factor in eq. (3) was taken to be $N = 1.0$ for the solid curve for ${}^{208}\text{Pb}$, $N = \frac{1}{2}$ for the dashed curve for ${}^{208}\text{Pb}$, and $N = \frac{2}{3}$ for the solid curve for ${}^{120}\text{Sn}$.

in the projectile frame. For the continuum states, the cross sections represent integration over ε in the range of 0–1.6 MeV. The angular distribution of the $\frac{7}{2}^-$ state is oscillatory, while that of the continuum is forward-peaked.

4. Theoretical analysis and discussion

4.1. ANGULAR DISTRIBUTIONS

The angular distributions obtained for the continuum states and the resonant $\frac{7}{2}^-$ state of ${}^7\text{Li}^*$ are analyzed by a DWBA method described in this subsection. We focus on the cases of ${}^{208}\text{Pb}$ and ${}^{120}\text{Sn}$ targets where we have the most extensive results. It was assumed that the continuum states are $s_{1/2}^+$ since the E1 contribution is known^{17,18)} to dominate in the radiative capture reaction, $\alpha(t, \gamma){}^7\text{Li}$. The transitions to the continuum and resonant states were then treated as E1 and E2 inelastic excitation of the projectile, respectively. These calculations were performed using E1 and E2 collective form factors. No final-state interaction between α and t and

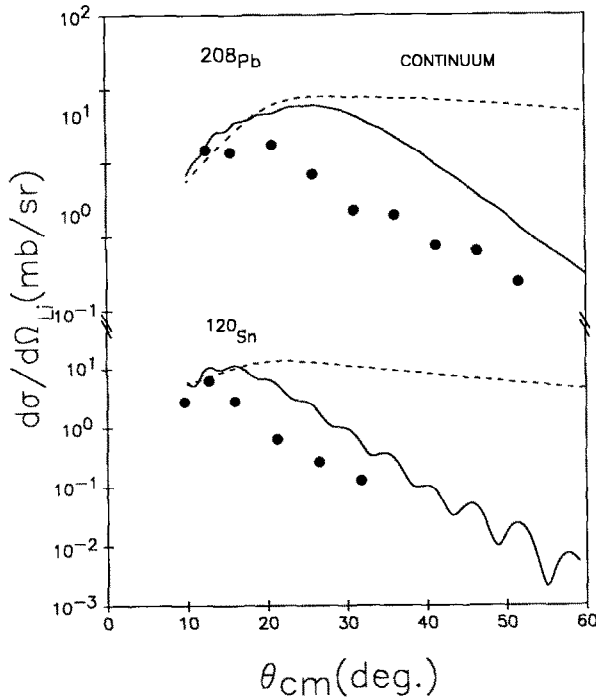


Fig. 21. Angular distributions of the continuum states of ${}^7\text{Li}$ taken with ${}^{208}\text{Pb}$ and ${}^{120}\text{Sn}$ targets. The solid curves are the results of the DWBA calculations with the collective E1 form factors, $\beta_n = \beta_c = 0.014$. The normalization factor in eq. (3) is $N = 1.8$ and $N = 2.9$ for the solid curves for ${}^{208}\text{Pb}$ and ${}^{120}\text{Sn}$, respectively. The dotted curves show the results for classical Coulomb excitation calculations²¹⁾. The reduced transition probability was determined from the astrophysical S -factor, $S = 0.065 \text{ MeV} \cdot \text{mb}$ [ref. 26)].

between these particles and the target was thus taken into account in the calculation. This description should be good for the excitation of a resonant state whose lifetime is sufficiently long so that the decay essentially takes place in the asymptotic region. The description, however, might not be good for the continuum transition. Nevertheless, we have used this approach to see how well a calculation based on simplified assumptions can account for the data.

With these approximations, the double-differential cross section is given in terms of the conventional DWBA cross section $d\sigma_l/d\Omega$ by

$$\frac{d^2\sigma}{d\Omega d\varepsilon} = N A_l(\varepsilon) \frac{d\sigma_l(\varepsilon)}{d\Omega} \quad (l = 1, 2), \quad (3)$$

where N is the normalization factor, and $A_l(\varepsilon)$ is the energy distribution of β_l^2 , the square of the deformation parameter β_l [ref. 19)]; namely

$$A_l(\varepsilon) = \frac{d\beta_l^2}{d\varepsilon}. \quad (4)$$

We generated $d\sigma_l(\varepsilon)/d\Omega$ with the program JPWKB²⁰⁾ using the optical potential parameters determined earlier (see sect. 3.1) for the two targets. The energy-integrated angular distribution $d\sigma/d\Omega$ can be obtained by integrating the double-differential cross section of eq. (3) over an appropriate energy interval of ε . For the resonant $\frac{7}{2}^-$ state at $\varepsilon = 2.16$ MeV, A_l may be taken as $\beta_l^2 \delta(\varepsilon - 2.16)$, since the transition strength is very sharply peaked at $\varepsilon = 2.16$ MeV. This is not the case for the continuum transition. Nevertheless, we assume here that $A_l = \beta_l^2 \delta(\varepsilon - 0.5)$, assuming that all the strength is concentrated at the peak position ($\varepsilon = 0.5$ MeV) of the continuum transition. We are here focusing our attention on fitting the shape of the angular distribution. An analysis of the energy distribution of the cross section will be presented in the next subsection in conjunction with astrophysical applications.

The calculated $d\sigma/d\Omega$ for the resonant and continuum transitions are shown by the solid curves in figs. 20 and 21, respectively. The deformation parameters for the nuclear and the Coulomb potentials were taken to be the same, i.e., $\beta_n = \beta_c$. In fig. 20, however, an additional theoretical cross section with $\beta_n = 1.5\beta_c$ is shown for the ^{208}Pb case while in fig. 21 the pure Coulomb excitation cross section, i.e., cross sections obtained by setting $\beta_n = 0$, and also neglecting the nuclear distortion effects are presented for both nuclei considered. The fit to the resonant state is fairly satisfactory for both targets. We remark that the interference between the nuclear and the Coulomb forces plays an essential role in obtaining the fit. The importance of the interference can be seen in the difference between two theoretical curves with $\beta_n/\beta_c = 1.0$ (the solid curve) and $\beta_n/\beta_c = 1.5$ (the dashed curve).

The calculations do not fit to the continuum as well as those obtained for the resonant state. An interesting aspect here is, however, that the theoretical continuum cross sections are dominated by the Coulomb excitation at forward angles of, say, $\theta < 17^\circ$. In fact, as seen in fig. 21, the calculated angular distribution with the nuclear plus Coulomb interactions is essentially identical to that obtained with only the Coulomb interaction inside 17° . This is what one expects from consideration of the Coulomb trajectory. For instance, in the case of ^{208}Pb , the classical distance of closest approach is more than 20 fm inside 20° which is considerably larger than the nuclear interaction radius of 14 fm. Note, however, that the experimental data do not follow the prediction of pure Coulomb excitations. This may indicate that, as we suggested before⁶⁾, a better treatment including three-body effects, e.g., the final-state interactions between two interacting clusters, which are influenced by the strong external field of the heavy target nucleus, is necessary.

4.2. COULOMB EXCITATION AND NUCLEAR ASTROPHYSICS

Coulomb excitation of continuum states around the particle separation energy has important astrophysical implications. The cross sections for radiative capture processes play a key role in nucleosynthesis in the Big Bang expansion as well as inside massive stars. However, conventional nuclear physics experiments can provide

the relevant data only by *extrapolation* since the astrophysical environment is unattainable in the laboratory. The inadequacy of the basic nuclear data has also been pointed out especially in conjunction with the solar neutrino problem and the mystery of primordial ${}^7\text{Li}$ synthesis^{22,23}). The Coulomb excitation of continuum states in breakup reactions may provide a unique handle on these problems. The astrophysical S -factor involved in the radiative capture cross section could be extracted from Coulomb breakup cross sections if the relative energies in the astrophysical domain were experimentally determined^{1,2}). Some attempts to calculate the Coulomb breakup cross sections based on the astrophysical S -factor have appeared in the literature^{24,25}).

There are two points which require both the experimentalists' attention and ingenuity in carrying out the theoretical scenario. First, one needs to be able to separate the contributions from Coulomb and nuclear breakup processes. By choosing an appropriate bombarding energy and detection angle, it should be possible to suppress nuclear breakup. Since the present data do not follow the prediction of Coulomb excitation, they are not so well-suited for this purpose. Secondly, one needs very high resolution to observe relative kinetic energies appropriate to the astrophysical range, typically on the order of keV. Although the spectrograph technique can safely satisfy the second condition under certain circumstances, the present experiment did not provide the required super sensitivity at the astrophysical energies (below 10 keV), as seen in sect. 3.6. Thus, we are not in a position to determine the astrophysical S -factor with much certainty. Nevertheless, we made an attempt to analyze the relative energy distributions based on eq. (3). Particularly, we study whether the β_i^2 distribution determined from available information on the astrophysical S -factor is consistent with the present data.

Applying the reciprocity theorem for the Coulomb breakup and the radiative capture, the reduced transition probability in units of $e^2 \text{fm}^2/\text{MeV}$ is given by

$$B(E1; \varepsilon) = \frac{9}{16\pi^3} \hbar c \frac{6}{7} \frac{mc^2}{E_\gamma^3} \varepsilon \sigma_{\text{at}}^c(\varepsilon) = \frac{81}{16\pi^2} e^2 R_0^2 \frac{d\beta_i^2}{d\varepsilon}. \quad (5)$$

Here, σ_{at}^c is the radiative capture cross section, mc^2 is the atomic mass unit and R_0 is the nuclear radius of ${}^7\text{Li}$. The astrophysical S -factor, $S(\varepsilon)$ is defined by

$$\sigma_{\text{at}}^c(\varepsilon) = \frac{1}{\varepsilon} e^{-2\pi\eta} S(\varepsilon), \quad (6)$$

with the Coulomb parameter $\eta = Z_\alpha Z_t e^2 / \hbar v$. Using eqs. (5) and (6), one can deduce the $d\beta_i^2/d\varepsilon$ needed to calculate the double-differential cross section (eq. (3)) and compare it with the experimental data.

Such comparisons are made in figs. 11 and 16 for the 12° spectra for ${}^{208}\text{Pb}$ and ${}^{120}\text{Sn}$, respectively. Two different S -factors were used in the calculations: the energy independent S -factor, $S(\varepsilon) = 0.065 \text{ MeV mb}$ as suggested by Griffiths *et al.*²⁶), and

the energy-dependent S -factor of Kajino, Bertsch and Kubo²⁷⁾). We introduced normalization factors in the calculations ranging from 0.64 to 0.85. Except at small relative energies, the gross features of the spectral shape are well reproduced by the present calculations. It should be noted that there is a discrepancy below $\epsilon = 500$ keV between data and calculation. The ^{208}Pb data (fig. 11) taken with a 3.0 msr collimator are expected to have an energy resolution of 140 keV (a coherent sum of the two factors given in figs. 18 and 19) at 500 keV. Taking this into consideration, however, does not eliminate the discrepancy.

One should be reminded that no post-Coulomb acceleration was taken into account in data reduction. Although the present data do not exhibit any strong post-Coulomb acceleration as discussed in sect. 3, it is interesting to see how the spectral shape is sensitive to this effect. For this purpose we examined two cases: $V_c = 0.3$ MeV and 1.0 MeV. The value of $V_c = 1.0$ MeV is probably too large to be accommodated by the data, while the possibility of $V_c = 0.3$ MeV cannot be excluded. Kinematical transformations were performed at the breakup point with c.m. energies obtained by subtracting $Z_i V_c$ ($i = \alpha$ or t) from the asymptotic energies. Fig. 22 shows the

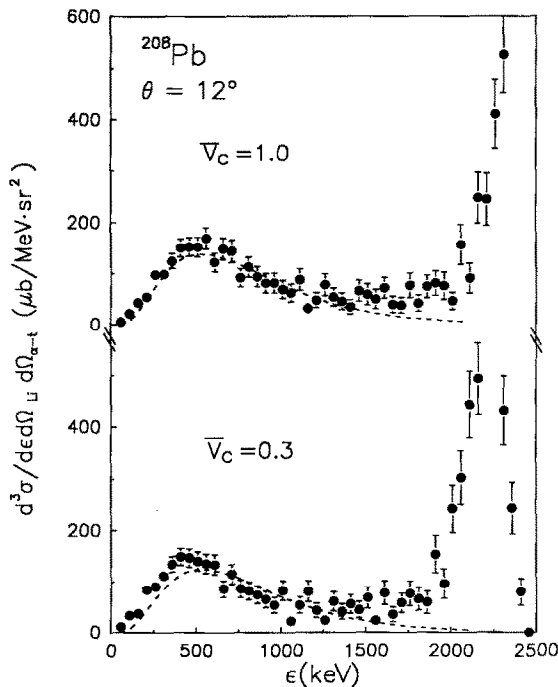


Fig. 22. Post-Coulomb acceleration effect on the relative energy distributions taken with ^{208}Pb at 12° . The kinematical transformations were made with $V_c = 1$ MeV (top) and $V_c = 0.3$ MeV (bottom), respectively. The dotted curves represent the Coulomb excitation calculations with the astrophysical S -factor, $S = 0.065$ MeV \cdot mb [ref. 26)]. Normalization factors of 1.0 and 0.9 are introduced to the calculations in the top and bottom part of the figure, respectively.

results. The discrepancy is reduced with $V_c = 0.3$ MeV and essentially removed with $V_c = 1$ MeV. However, note that the $\frac{7}{2}^-$ state appears at the wrong energy, especially in the case of $V_c = 1$ MeV. The assumption of a post breakup acceleration is clearly unphysical for this long-lived state.

5. Conclusions

A new particle correlation technique suitable for studying nuclear states around the particle threshold has been applied to the ${}^7\text{Li}$ system. αt correlations with relative kinetic energies ranging from 0 to 2.4 MeV were measured. In addition to the $\frac{7}{2}^-$ state at 4.63 MeV, a continuous distribution of the αt relative energies was studied without any detection threshold. A pronounced bump was found, which starts at the αt particle threshold, peaks around 500 keV, and extends toward higher excitation energies. Under the present experimental conditions, the finite opening angle of the spectrograph and the finite target thickness did not distort the spectral shape of the continuum, but did degrade the energy resolution.

The excitation of the $\frac{7}{2}^-$ resonant state is governed by a strong interference between the Coulomb and nuclear forces. Although the present DWBA calculations suggested that the continuum should be excited predominantly by the Coulomb interaction inside 17° , the data do not follow such predictions. At small relative energies, there are discrepancies between the data and the spectra deduced from radiative capture cross sections. A more microscopic calculation of the continuum bump, such as a three-body calculation, may be necessary to explain the data.

In the future, two points need to be clarified regarding the continuum: (1) spin orientation of ${}^7\text{Li}^*$ and (2) post Coulomb acceleration effects. In the calculations, the continuum was assumed to be $s_{1/2}^+$. With this spin, there cannot be any polarization of the excited ${}^7\text{Li}$. However, this assumption may not be correct. In general, if non-zero relative angular momenta between an α and a triton are involved in the continuum, they could produce a polarization. The possibility of spin orientation could be checked by measuring the in-plane and out-of-plane asymmetry in the correlation cross section. From the analysis of the nuclear events corresponding to $\varepsilon = 0$, we found no strong evidence for post-breakup acceleration of the fragments in the Coulomb field of the target ($V_c \leq 350$ keV). This is consistent with the αd correlation study with a magnetic spectrograph in the breakup of ${}^6\text{Li}$ at 156 MeV [ref. ²⁸]. However, this seems to contradict some observations ^{12,29}) made with the telescope method which showed a forward-backward asymmetry in the fragment spectra. Further studies are necessary to resolve these observations.

The present technique, which was mentioned by Enge ⁷), one of the inventors of the magnetic spectrographs, plays a complementary role to the telescope method and seems very useful in various purposes in nuclear physics ⁵). The energy resolution at small relative energies is very sensitive to the finite opening angle and the finite target thickness. To observe small relative energies with great sensitivity, e.g., for

astrophysical applications, it is desirable to combine this technique with particle-tracking capability and a thin target. A dispersion-matched beam would also be necessary for a radio-frequency modulated beam. For a wide range of applications of the present technique to two/three particle correlation experiments, it would be desirable to develop a *large scale* (large K -value), ultra broad range magnetic spectrograph exhibiting an energy acceptance ≥ 10 , high resolving power (less aberration), large solid angle with particle-tracking capabilities such as ray-tracing, and stigmatic focusing.

The authors would like to thank Professor Taro Tamura for his encouragement and contributions to this study. This work was partially supported by the U.S. Department of Energy under grant DE-FG05-86ER40256 and The Robert A. Welch Foundation under grant No. A-972.

Appendix

KINEMATICS

A number of papers regarding the use of jacobians in kinematical transformations of event-by-event data have appeared in the literature^{15,30}). A general discussion of the kinematical transformations relevant to the present experiment has been given by Fuchs¹⁵). In view of the importance of the problems, we will summarize the details of the event-by-event transformation used in our data analysis.

The present purpose is to make an event-by-event transformation from the laboratory cross section, $d\sigma/dE_\alpha dE_t d\Omega_\alpha d\Omega_t$, to the cross section in the projectile frame, $d\sigma/d\varepsilon d\Omega_{\alpha t} d\Omega_{Li}$. Let us start with a complete transformation, i.e.,

$$\frac{d\sigma}{d\varepsilon dE_{tot} d\Omega_{\alpha t} d\Omega_{Li}} = \frac{d\sigma}{dE_\alpha dE_t d\Omega_\alpha d\Omega_t} J_{tot}, \quad (A.1)$$

where the total jacobian J_{tot} is

$$J_{tot} = \frac{\partial(E_\alpha, E_t, \Omega_\alpha, \Omega_t)}{\partial(\varepsilon, E_{tot}, \Omega_{\alpha t}, \Omega_{Li})} = \frac{\mu p_{rel} \mu_T p_T}{m_\alpha p_\alpha m_t p_t}. \quad (A.2)$$

Here, E_{tot} is the total kinetic energy, μ is the reduced mass for the $\alpha + t$ system, p_{rel} is the αt relative momentum, p_t is the target momentum relative to ${}^7\text{Li}$, and μ_T is the reduced mass for the target + ${}^7\text{Li}$ system, i.e.,

$$\begin{aligned} \mu &= \frac{12}{7}, \\ p_{rel} &= \mu(p_\alpha/m_\alpha - p_t/m_t), \\ \mu_T &= 7m_T/(7 + m_T), \\ p_T &= 7P/(7 + m_T) - p_\alpha - p_t. \end{aligned} \quad (A.3)$$

The quantity m_T is the target mass and P is the total momentum, which is equal to the incident projectile momentum in the laboratory system and is equal to zero in the c.m. system. The total kinetic energy E_{tot} is given by $E_{\text{tot}} = E_\alpha + E_t + E_T$ or $E_{\text{tot}} = E_0 + Q$ with the appropriate reaction Q -value. Multiplying eq. (A.1) by

$$\Delta \varepsilon \Delta E_{\text{tot}} = \frac{\partial(\varepsilon, E_{\text{tot}})}{\partial(E_\alpha, E_t)} \Delta E_\alpha \Delta E_t, \quad (\text{A.4})$$

we obtain

$$\frac{d\sigma}{d\varepsilon dE_{\text{tot}} d\Omega_{\alpha t} d\Omega_{\text{Li}}} \Delta \varepsilon \Delta E_{\text{tot}} = \frac{d\sigma}{dE_\alpha dE_t d\Omega_\alpha d\Omega_t} J_{\text{tot}} \frac{\partial(\varepsilon, E_{\text{tot}})}{\partial(E_\alpha, E_t)} \Delta E_\alpha \Delta E_t. \quad (\text{A.5})$$

For elastic/inelastic breakup events, E_{tot} can be treated as a constant because the reaction Q -value is given by $Q_{\text{el}} = (m_{\text{Li}} - m_\alpha - m_t)c^2$ for the elastic breakup and $Q_{\text{inel}} = Q_{\text{el}} - E_x$ for the inelastic breakup with a target excitation energy, E_x . The target recoil energy, E_T , is constant at each detection angle. Multiplying eq. (A.5) by $d(E_{\text{tot}} - A)$ and integrating over E_{tot} , we are left with

$$\begin{aligned} & \left[\frac{d\sigma}{d\varepsilon d\Omega_{\alpha t} d\Omega_{\text{Li}}} \right]_{E_{\text{tot}}=A} \Delta \varepsilon \\ &= \left[\frac{d\sigma}{dE_{\alpha(t)} d\Omega_\alpha d\Omega_t} \right]_{E_{\text{tot}}=A=E_\alpha+E_t+E_T} \left[J_{\text{tot}} \frac{\partial(\varepsilon, E_{\text{tot}})}{\partial(E_\alpha, E_t)} \right] \Delta E_{\alpha(t)}. \end{aligned} \quad (\text{A.6})$$

Eq. (A.6) shows that the cross section in the projectile frame in the interval $\varepsilon - \varepsilon + \Delta \varepsilon$ is obtained by multiplying the laboratory cross section in the interval $E_\alpha - E_\alpha + \Delta E_\alpha$ ($E_t - E_t + \Delta E_t$) with the event-by-event jacobian, J , the term in the parentheses. Namely,

$$J = J_{\text{tot}} \frac{\partial(\varepsilon, E_{\text{tot}})}{\partial(E_\alpha, E_t)} = \frac{\partial(\Omega_\alpha, \Omega_t)}{\partial(\Omega_{\alpha t}, \Omega_{\text{Li}})}. \quad (\text{A.7})$$

The explicit form of J is given by

$$J = \frac{\mu p_{\text{rel}} \mu_T p_T}{m_\alpha p_\alpha m_t p_t} \begin{vmatrix} \frac{\partial \varepsilon}{\partial E_\alpha} & \frac{\partial \varepsilon}{\partial E_t} \\ \frac{\partial E_{\text{tot}}}{\partial E_\alpha} & \frac{\partial E_{\text{tot}}}{\partial E_t} \end{vmatrix}, \quad (\text{A.8})$$

where

$$\begin{aligned} \frac{\partial \varepsilon}{\partial E_{\alpha(t)}} &= \mu(1/m_{\alpha(t)} - \mathbf{p}_\alpha \cdot \mathbf{p}_t / m_{t(\alpha)} p_{\alpha(t)}^2) \\ \frac{\partial E_{\text{tot}}}{\partial E_{\alpha(t)}} &= \frac{1}{m_T} \left[m_{\alpha(t)} + m_T - m_{\alpha(t)} \frac{\mathbf{p}_{\alpha(t)} \cdot (\mathbf{P} - \mathbf{p}_{t(\alpha)})}{p_{\alpha(t)}^2} \right]. \end{aligned} \quad (\text{A.9})$$

At $\theta_\alpha = \theta_t$, which is the case in our experiment within the finite solid angle of the spectrograph, we have finally

$$J = \frac{\mu p_{\text{rel}} \mu_T p_T}{m_\alpha p_\alpha m_t p_t} p_{\text{rel}} \left[\frac{1}{p_\alpha} \frac{\partial E_{\text{tot}}}{\partial E_t} + \frac{1}{p_t} \frac{\partial E_{\text{tot}}}{\partial E_\alpha} \right]. \quad (\text{A.10})$$

References

- 1) H. Rebel, Workshop on nuclear reaction cross sections of astrophysical interest, Kernforschungszentrum Karlsruhe, Report 1985, unpublished
- 2) G. Baur, C.A. Bertulani and H. Rebel, Nucl. Phys. **A458** (1986) 188
- 3) D.L. Disdier, G.C. Ball, O. Hässer and R.E. Warner, Phys. Rev. Lett. **27** (1971) 1391
- 4) A. Baden, H.H. Gutbrod, H. Löhner, M.R. Mainer, A.M. Poskanzer, T. Renner, H. Riedesel, H.G. Ritter, H. Spieler, A. Warwick, F. Weik and H. Weiman, Nucl. Instr. Meth. **203** (1982) 189
- 5) H. Utsunomiya, Y.-W. Lui and R.P. Schmitt, Nucl. Instr. Meth. **A278** (1989) 744
- 6) H. Utsunomiya, R.P. Schmitt, Y.-W. Lui, D.R. Haenni, H. Dejbakhsh, L. Cooke, P. Heimberg, A. Ray, T. Tamura and T. Udagawa, Phys. Lett. **B211** (1988) 24
- 7) H.A. Enge, Nucl. Instr. Meth. **28** (1964) 119
- 8) J.E. Spencer and H.A. Enge, Nucl. Instr. Meth. **49** (1967) 181
- 9) F.H. Schmidt, H. Fauska and J.W. Orth, Nuclear electronics III (International atomic energy agency, Vienna, 1962) p. 381
- 10) S. Kobayashi, S. Motonaga, Y. Chiba, K. Katori, A. Stricker, T. Fujisawa and T. Wada, J. Phys. Soc. Jpn. **29** (1970) 1
- 11) L.T. Chua, F.D. Becchetti, J. Jänecke and F.L. Milder, Nucl. Phys. **A273** (1976) 243
- 12) A.C. Shotton, A.N. Bice, J.M. Wouters, W.D. Rae and J. Cerny, Phys. Rev. Lett. **46** (1981) 12
- 13) M.A. Bernstein and W.A. Friedman, Phys. Rev. **C31** (1985) 843
- 14) J. Pochodzalla, C.K. Gelbke, C.B. Chitwood, D.J. Fields, W.G. Lynch, M.B. Tsang and W.A. Friedman, Phys. Lett. **B175** (1986) 275
- 15) H. Fuchs, Nucl. Instr. Meth. **200** (1982) 361
- 16) C.P. Browne, Bull. Am. Phys. Soc. **2** (1957) 350
- 17) T.A. Tombrello and P.D. Parker, Phys. Rev. **131** (1963) 2582
- 18) T. Kajino and A. Arima, Phys. Rev. Lett. **52** (1984) 739;
T. Kajino, Nucl. Phys. **A460** (1986) 559
- 19) T. Tamura, Rev. Mod. Phys. **37** (1965) 679
- 20) T. Kim, T. Udagawa, D.H. Feng and T. Tamura, Computer code JPWKB, unpublished
- 21) K. Alder, A. Bohr, T. Huus, B. Mottelson and A. Winther, Rev. Mod. Phys. **28** (1956) 432
- 22) T. Kajino, H. Toki and S.M. Austin, Astrophys. J. **319** (1987) 531
- 23) U. Schröder, A. Redder, C. Roles, R.E. Azuma, L. Buchmann, C. Campbell, J.D. King and T.R. Donoghue, Phys. Lett. **B192** (1987) 55
- 24) A.C. Shotton, V. Rapp, T. Davinson, D. Branford, N.E. Sanderson and M.A. Nagarajan, Phys. Rev. Lett. **53** (1984) 1539
- 25) D.K. Srivastava, D.N. Basu and H. Rebel, Phys. Rev. **C38** 2148 (1988); Phys. Lett. **B206** (1988) 391
- 26) G.M. Griffiths, R.A. Morrow, P.J. Riley and J.B. Warren, Can. J. Phys. **39** (1961) 1391
- 27) T. Kajino, G.F. Bertsch and K.-I. Kubo, Phys. Rev. **C37** (1988) 512
- 28) J. Kiener, H.J. Gils, H. Rebel and G. Baur, Z. Phys. **A332** (1989) 359
- 29) J. Hesselbarth, S. Khan, Th. Kihm and K.T. Knöpfle, Z. Phys. **A331** (1988) 365
- 30) H. Ho and P.L. Gonthier, Nucl. Instr. Meth. **190** (1981) 75